On the geometry of fracture and frustration

Koning, V.

Part II

TOROIDAL NEMATICS

In this part, we present a theoretical study of director fields in toroidal (rather than spherical) geometries with degenerate planar boundary conditions. In contrast to spherical nematics in Part I, the topology does not induce defects in nematic toroids. However, we do find spontaneous chirality: despite the achiral nature of nematics the director configuration shows a handedness if the toroid is thick enough. In the chiral state the director field displays a double twist, whereas in the achiral state there is only bend deformation. The critical thickness increases as the difference between the twist and saddle-splay moduli grows. A positive saddle-splay modulus prefers alignment along the meridians of the bounding torus, and hence promotes a chiral configuration. The chiral-achiral transition mimics the order-disorder transition of the mean-field Ising model. The role of the magnetisation in the Ising model is played by the degree of twist. The role of the temperature is played by the aspect ratio of the torus. Remarkably, an external field does not break the chiral symmetry explicitly, but shifts the transition. In the case of toroidal cholesterics, we do find a preference for one chirality over the other – the molecular chirality acts as a field in the Ising analogy. Remarkably, an external field does not break the chiral symmetry explicitly, but shifts the transition. Finally, we compare theoretical findings with experimental observations of chirality in toroidal nematic droplets.

4

CHIRAL SYMMETRY BREAKING

4.1 INTRODUCTION

The liquid crystal in a common display is twisted due to the orientation of the molecules at the confining glass plates. By manipulating this twist using electric fields, an image can be generated. More exotic structures can emerge when the liquid crystal is confined by curved rather than flat surfaces. The topology and geometry of the bounding surface can drive the system into structures that would not be achieved without the presence of external fields. In this sense, the shape of the surface plays a role akin to that of an external field. Thus, under confinement by curved surfaces, the molecules can self-assemble into complex hierarchical structures with emergent macroscopic properties not observed for flat liquid crystal cells. However, the design principles and properties of structures generated by this geometric route are still largely unknown. As discussed in Part I, spherical nematics have been widely studied from experimental, theoretical, and simulation points of view and their intriguing technological potential for divalent nanoparticle assembly has been already demonstrated [20]. In contrast, there are virtually no controlled experiments with ordered media in confined volumes with handles, even though there has been much interest in the interplay between order and toroidal geometries [94, 7, 43, 28, 27, 6, 114, 84, 10]. Alberto Fernanez-Nieves and co-workers experimentally generate stable toroidal droplets of a nematic liquid crystal, using a continuous host with a yield stress. This approach allows them to perform unique experiments that probe nematic materials confined within droplets that are topologically different from the sphere. We observe that the toroidal nematic droplets formed are defect-free. However, polarised microscopy reveals a twisted nematic orientation in droplets with planar degenerate (tangential) boundary conditions, despite the achiral nature of nematics. This phenomenon, which we will iden-

tify as spontaneous chiral symmetry breaking[1], is subject of theoretical study in this chapter. The chirality of nematic toroids is displayed by the the local average orientation of the nematic molecules, called the director field and indicated by the unit vector $\mathbf{n}$. Motivated by experiment, we will assume this director field to be aligned in the tangent plane of the bounding torus. Fig. 36a shows an achiral nematic toroid which has its fieldlines aligned along the azimuthal direction, $\hat{\phi}$. In contrast, the chiral nematic toroids in Figs. 36b and 36c show a right and left handedness, respectively, when following the fieldlines anticlockwise (in the azimuthal direction). The origin of the chirality lies in two elastic ef-

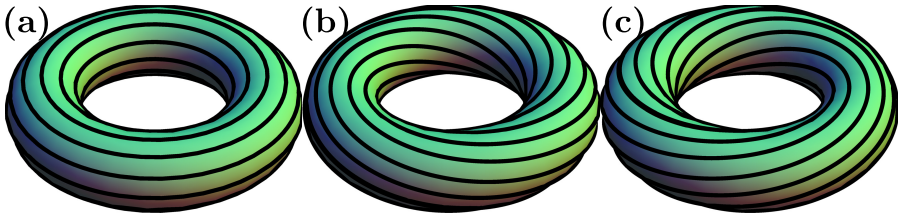

Figure 36: Schematic of (a) achiral, (b) righthanded and (c) lefthanded toroidal nematic liquid crystals. The black lines are director field lines on the bounding torus.

fects of geometric confinement. Firstly, there is a trade-off between bend and twist deformations. Secondly, another type of director distortion called saddle-splay couples the director to the curvature of the boundary, and can consequently favour the chiral state.

These nematic toroids share similarites with polymer bundles [5, 43, 61, 48, 60, 87, 31]. In fact, twisted DNA toroids have been analysed with liquid crystal theory [43, 99, 87]. Under the appropriate solvent conditions DNA condenses into toroids [53, 5]. These efficient packings of genetic material are interesting as vehicles in therapeutic gene delivery; it has been argued [43] that a twist in DNA toroids, for which there are indications both in simulations [96, 98] and experiments [14], would unfold more slowly and could therefore be beneficial for this delivery process. Thus, besides a way to engineer complex structures, the theory of geometrically confined liquid crystals may also provide understanding of biological systems.

1 Technically, it is spontaneous *achiral* symmetry breaking since the symmetry is the *lack* of chirality. However, we will conform to the standard convention.

The organisation of this chapter is as follows. In section 4.2 we will discuss our calculational method which involves a single variational *Ansatz* only for the director fields of both chiral and achiral toroidal nematics. In section 4.3 we will consider its energetics in relation to the slenderness, elastic anisotropies, cholesteric pitch and external fields, and discuss the achiral-chiral transition in the light of the mean field treatment of the Ising model. In section 4.4 we compare these theoretical results with experimental measurements of the twist in toroidal nematic droplets. Finally, we conclude in section 4.5.

4.2 TOROIDAL DIRECTOR FIELDS

4.2.1 *Free energy of a nematic toroid*

We will study the general case in which the director lies in the tangent plane of the boundary assuming that the anchoring is strong so that the only energy arises from elastic deformations captured by the Frank free energy functional [18, 40]:

$$\begin{aligned} F[\mathbf{n}(\mathbf{x})] = \frac{1}{2}\int \mathrm{d}V \Big(& K_1 (\nabla\cdot\mathbf{n})^2 \\ & + K_2 (\mathbf{n}\cdot\nabla\times\mathbf{n})^2 + K_3 (\mathbf{n}\times\nabla\times\mathbf{n})^2 \Big) \\ & - K_{24}\int \mathbf{dS}\cdot(\mathbf{n}\nabla\cdot\mathbf{n} + \mathbf{n}\times\nabla\times\mathbf{n}), \end{aligned} \tag{141}$$

where $\mathrm{d}\mathbf{S} = \boldsymbol{\nu}\,\mathrm{d}S$ is the area element, with $\boldsymbol{\nu}$ the unit normal vector (outward pointing) and where $\mathrm{d}V$ is the volume element. Due to the anisotropic nature of the nematic liquid crystal, this expression contains three bulk elastic moduli, K_1, K_2, K_3, rather than a single one for fully rotationally symmetric systems. In addition, there is a surface elastic constant K_{24}. K_1, K_2, K_3 and K_{24} measure the magnitude of splay, twist, bend and saddle-splay distortions, respectively. We now provide a geometrical interpretation of the saddle-splay distortions. Firstly, observe that under perfect planar anchoring conditions $\mathbf{n}\cdot\boldsymbol{\nu} = 0$ and so the first term in the saddle-splay energy does not contribute:

$$F_{24} = -K_{24}\int \mathrm{d}S\,\boldsymbol{\nu}\cdot(\mathbf{n}\times\nabla\times\mathbf{n}). \tag{142}$$

This remaining term in the saddle-splay energy is often rewritten as

$$F_{24} = K_{24} \int \mathrm{d}S \; \boldsymbol{\nu} \cdot (\mathbf{n} \cdot \nabla) \, \mathbf{n}. \tag{143}$$

because

$$\begin{aligned} (\mathbf{n} \times \nabla \times \mathbf{n})_a &= \epsilon_{abc} n_b \epsilon_{cpq} \partial_p n_q \\ &= (\delta_{ap}\delta_{bq} - \delta_{aq}\delta_{bp}) \, n_b \partial_p n_q \\ &= -n_b \partial_b n_a, \end{aligned} \tag{144}$$

where in the last line one uses that $0 = \partial_a (1) = \partial_a (n_b n_b) = 2 n_b \partial_a n_b$. In other words, the bend is precisely the curvature of the integral curves of $\mathbf{n}$. Employing the product rule of differention $0 = \partial_a (\nu_b n_b) = \nu_b \partial_a n_b + n_b \partial_a \nu_b$ yields

$$F_{24} = -K_{24} \int \mathrm{d}S \; \mathbf{n} \cdot (\mathbf{n} \cdot \nabla) \, \boldsymbol{\nu}. \tag{145}$$

Upon writing $\mathbf{n} = n_1 \boldsymbol{e}_1 + n_2 \boldsymbol{e}_2$, with $\boldsymbol{e}_1$ and $\boldsymbol{e}_1$ two orthonormal basis vectors in the plane of the surface, one obtains

$$F_{24} = K_{24} \int \mathrm{d}S \; n_i L_{ij} n_j, \tag{146}$$

where we note that $i, j = 1, 2$ (rather than running till 3). Thus the nematic director couples to the extrinsic curvature tensor [37], defined as

$$L_{ij} = -\boldsymbol{e}_i \cdot (\boldsymbol{e}_j \cdot \nabla) \, \boldsymbol{\nu}. \tag{147}$$

If $\boldsymbol{e}_1$ and $\boldsymbol{e}_2$ are in the directions of principal curvatures, κ_1 and κ_2, respectively, one finds

$$F_{24} = K_{24} \int dS \left(\kappa_1 n_1^2 + \kappa_2 n_2^2 \right). \tag{148}$$

We conclude that the saddle-splay term favours alignment of the director along the direction with the smallest principal curvature if $K_{24} > 0$. The controversial surface energy density $K_{13} \mathbf{n} \nabla \cdot \mathbf{n}$ is sometimes incorporated in eq. (141), but is in our case irrelevant, because the normal vector is perpendicular to $\mathbf{n}$, and so $\mathbf{n} \cdot \boldsymbol{\nu} = 0$.

We will consider a nematic liquid crystal confined in a handle body bounded by a torus given by the following implicit equation for the cartesian coordinates x, y, and z:

$$\left(R_1 - \sqrt{x^2 + y^2} \right)^2 + z^2 \leq R_2^2. \tag{149}$$

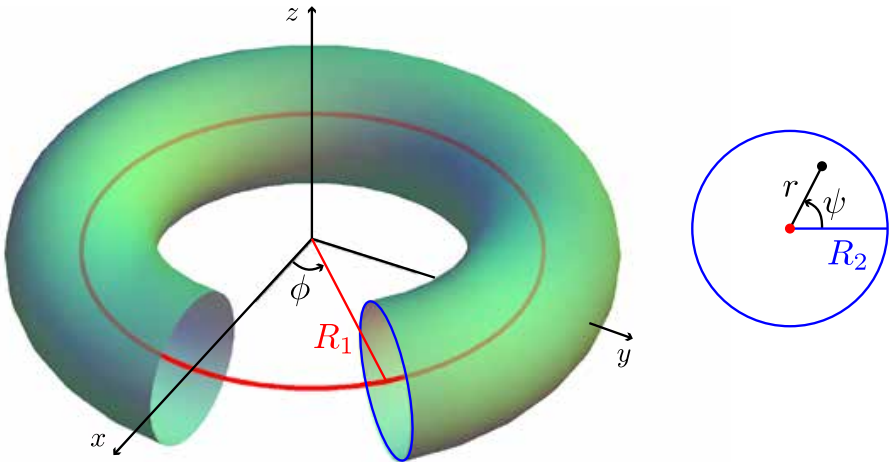

Figure 37: *Left panel*: Schematic of the boundary of the geometry specified eq. (149) including graphical definitions of ϕ and R_1. The torus characterised by a large (red) and a small (blue) circle. The large circle, or centerline, has radius R_1. *Right panel*: Schematic of a cut including graphical definitions of r, ψ and R_2.

Here, R_1 and R_2 are the large and small radii, respectively, of the circles that characterise the outer surface: a torus obtained by revolving a circle of radius R_2 around the z-axis (Fig. 37). We can conveniently parametrise this solid torus by the coordinates $r \in [0, R_2]$, $\phi \in [0, 2\pi)$ and $\psi \in [0, 2\pi)$ (illustrated in Fig. 37):

$$x = (R_1 + r\cos\psi)\cos\phi, \tag{150}$$

$$y = (R_1 + r\cos\psi)\sin\phi, \tag{151}$$

$$z = r\sin\psi. \tag{152}$$

The metric reads:

$$g_{\mu\nu} = \begin{pmatrix} 1 & 0 & 0 \\ 0 & (R_1 + r\cos\psi)^2 & 0 \\ 0 & 0 & r^2 \end{pmatrix}, \tag{153}$$

with $\mu, \nu \in \{r, \phi, \psi\}$. It follows that $\mathbf{dS} = \boldsymbol{\nu}\sqrt{g}\,\mathrm{d}\psi\,\mathrm{d}\phi$ and $\mathrm{d}V = \sqrt{g}\,\mathrm{d}r\,\mathrm{d}\psi\,\mathrm{d}\phi$, where $g = \det g_{\mu\nu}$.

For a torus the ϕ and ψ directions are the principal directions. The curvature along the ψ direction is everywhere negative (measured with respect to the outward pointing normal) and the smallest of the two, so when $K_{24} > 0$, the director tends to wind along the small circle with radius R_2 (*i.e.* meridian).

4.2.2 *Double twist*

To minimise the Frank energy we formulate a variational *Ansatz* built on several simplifying assumptions [43]. We consider a director field which has no radial component (*i.e.* $n_r = 0$), is tangential to the centerline ($r = 0$), and is independent of ϕ. Furthermore, since we expect the splay (K_1) distortions to be unimportant, we first take the field to be divergence free (*i.e.*$\nabla \cdot \mathbf{n} = 0$). Recalling that in curvilinear coordinates the divergence is $\nabla \cdot \mathbf{n} = \frac{1}{\sqrt{g}} \partial_\mu \left(\sqrt{g} n^\mu \right)$, we write :

$$n_\psi = \frac{f\left(r\right) R_1}{\sqrt{g_{\phi\phi}}}, \tag{154}$$

where the other terms in $\sqrt{g}$ play no role as they are independent of ψ. The ϕ-component of the director follows from the normalisation condition. For the radial dependence of $f\left(r\right)$ we make the simplest choice:

$$f\left(r\right) = \frac{\omega r}{R_2}, \tag{155}$$

and obtain

$$n_\psi = \omega \frac{\xi r / R_2}{\xi + \frac{r}{R_2} \cos\psi}, \tag{156}$$

where we have introduced $\xi \equiv R_1 / R_2$, the slenderness or aspect ratio of the torus. The variational parameter ω governs the chirality of the toroidal director field. If $\omega = 0$ the director field corresponds to the axial configuration (Fig 36a). The sign of ω determines the chirality: right handed when $\omega > 0$ (Fig. 36c) and left handed when $\omega < 0$ (Fig. 36b). The magnitude of ω determines the degree of twist. Note that the direction of twist is in the radial direction, as illustrated in Fig. 38. Therefore the toroidal nematic is doubly twisted, resembling the cylindrical building blocks of the blue phases [18, 40]. It may be useful to relate ω with a quantity at the surface, say the angle, α, that the director makes with $\hat{\phi}$. For the *Ansatz*, this angle will be different depending on whether one measures at the inner or outer part of the torus, but for large ξ we find

$$\omega \approx n_\psi \left(r = R_2\right) = \sin\alpha. \tag{157}$$

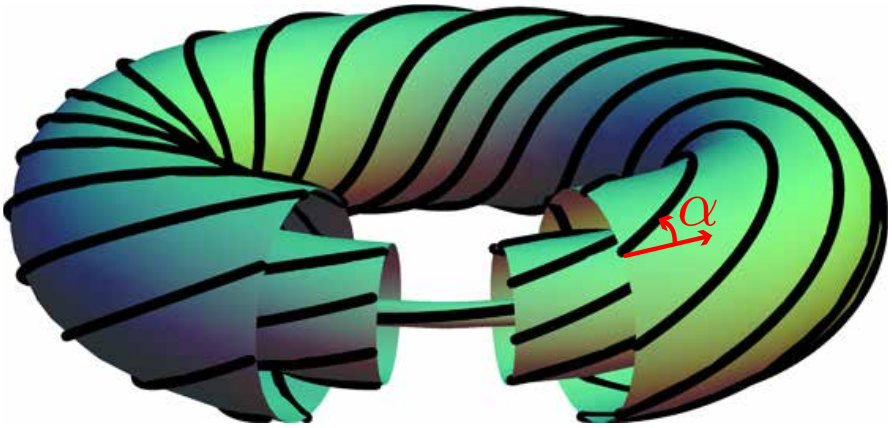

Figure 38: Schematic of the *Ansatz* for the director fieldlines ($\omega = 0.6$ and $\xi = 3$), displaying a twist when going radially outward, including a graphical definition of α.

4.3 CHIRAL SYMMETRY BREAKING

4.3.1 *Results for divergence-free field*

Since ω only determines the chirality of the double-twisted configuration but not the amount of twist, the free energy is invariant under reversal of the sign of ω, *i.e.* $F(-\omega) = F(\omega)$. This mirror symmetry allows us to write down a Landau-like expansion in which F only contains even powers of ω,

$$F = a_0(\{K_i\}, \xi) + a_2(\{K_i\}, \xi)\,\omega^2 + a_4(\{K_i\}, \xi)\,\omega^4 + \mathcal{O}\left(\omega^6\right) \tag{158}$$

where $\{K_i\} = \{K_1, K_2, K_3, K_{24}\}$, the set of elastic constants. If the coefficient $a_2 > 0$, the achiral nematic toroid ($\omega_{eq} = 0$) corresponds to the minimum of F provided that $a_4 > 0$. In contrast, the mirror symmetry is broken spontaneously whenever $a_2 < 0$ (and $a_4 > 0$). The achiral-chiral critical transition at $a_2 = 0$ belongs to the universality class of the mean-field Ising model. Therefore, we can immediately infer that the value of the critical exponent β in $\omega_{eq} \sim (-a_2)^{\beta}$ is $\frac{1}{2}$. To obtain the dependence of the coefficients a_i

on the elastic constants and ξ, we need to evaluate the integral in eq. (141). We find for the bend, twist and saddle-splay energies:

$$\frac{F_3}{K_3R_1} = 2\pi^2\left(\xi - \sqrt{\xi^2-1}\right)/\xi + \pi^2\frac{\xi\left(1-9\xi^2+6\xi^4+6\xi\sqrt{\xi^2-1}-6\xi^3\sqrt{\xi^2-1}\right)}{\left(\xi^2-1\right)^{\frac{3}{2}}}\omega^2 + \mathcal{O}\left(\omega^4\right), \tag{159}$$

$$\frac{F_2}{K_2R_1} = 4\pi^2\frac{\xi^3}{\left(\xi^2-1\right)^{\frac{3}{2}}}\omega^2 + \mathcal{O}\left(\omega^6\right), \tag{160}$$

$$\frac{F_{24}}{K_{24}R_1} = -4\pi^2\frac{\xi^3}{\left(\xi^2-1\right)^{\frac{3}{2}}}\omega^2. \tag{161}$$

Though the bend and twist energies are Taylor expansions in ω, the saddle-splay energy is exact. The large ξ asymptotic behavior of the elastic energy reads[2]:

$$\frac{F}{K_3R_1} \approx \frac{\pi^2}{\xi^2} + 4\pi^2\left(k - \frac{5}{16\xi^2}\right)\omega^2 + \frac{\pi^2}{2}\omega^4 + \mathcal{O}\left(\omega^6\right), \tag{162}$$

where $k \equiv \frac{K_2-K_{24}}{K_3}$ is the elastic anisotropy in twist and saddle-splay. The achiral configuration contains only bend energy. For sufficiently thick toroids, bend distortions are exchanged with twist and the mirror symmetry is indeed broken spontaneously (Fig. 39). Interestingly, if $K_{24} > 0$ the saddle-splay deformations screen the cost of twist. If $K_{24} < 0$ on the other hand, there is an extra penalty for twisting. Setting the coefficient of the ω^2 term equal to zero yields the phase boundary:

$$k_c = \frac{-1+9\xi_c^2-6\xi_c^4-6\xi_c\sqrt{\xi_c^2-1}+6\xi_c^3\sqrt{\xi_c^2-1}}{4\xi_c^2} \approx \frac{5}{16\xi_c^2} \qquad \text{if } \xi \gg 1. \tag{163}$$

Fig. 40 shows the phase diagram as a function of ξ and k. It is interesting to look at the critical behavior. The degree of twist close to the transition is

$$\alpha_{eq} \approx \omega_{eq} \approx 2\left(\frac{5}{16\xi^2} - k\right)^{1/2}, \tag{164}$$

2 The fourth order term in the bend energy for general ξ, that reduces to $\frac{\pi^2}{2}K_3R_2\xi\omega^4$ in eq. (162), is not given in eq. (159), because it is too lengthy.

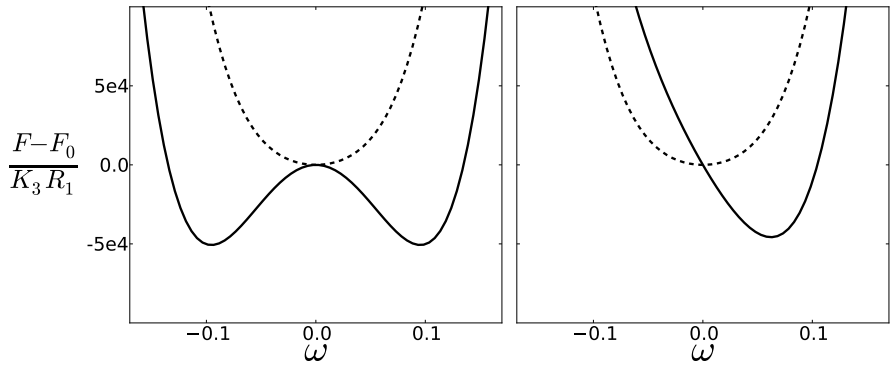

Figure 39: *Left panel:* The free energy as a function of ω for $\xi = 6$ (dashed) and $\xi = 5$ (solid), when $(K_2 - K_{24})/K_3 = 10^{-2}$. For $\xi = 5$ the chiral symmetry is broken spontaneously: the minimum values of the energy occurs for a nonzero ω. *Right panel:* The free energy as a function of ω for $q = 0$ (dashed) and $qR_2 = 10^{-3}$ (solid), when $\xi = 6$, $(K_2 - K_{24})/K_3 = 10^{-2}$ and $K_2/K_3 = 0.3$. For $qR_2 = 10^{-3}$ the chiral symmetry is broken explicitly: the minimum value of the energy occurs for a nonzero ω, because F contains a term linear in ω.

where we have used that $\sin\alpha_{eq} \approx \alpha_{eq}$ for small α_{eq}. Upon expanding $\xi = \xi_c + \delta\xi$ (with $\delta\xi < 0$) and $k = k_c + \delta k$ (with $\delta k < 0$) around their critical values ξ_c and k_c, respectively, we obtain the following scaling relations:

$$\alpha_{eq} \approx \frac{\sqrt{5}}{2}\left(-\frac{\delta\xi}{\xi_c^3}\right)^{1/2} \tag{165}$$

$$\alpha_{eq} \approx 2\left(-\delta k\right)^{1/2} \tag{166}$$

while keeping k and ξ fixed, respectively. Eqs. (165) and (166) are analogues to $m_{eq} \sim (-t)^{1/2}$, relating the equilibrium magnetisation, m_{eq} (in the ferromagnetic phase of the Ising model in Landau theory), to the reduced temperature, t.

4.3.2 *Effects of external fields and cholesteric pitch*

Due to the inversion symmetry of nematics, $F[\mathbf{n}] = F[-\mathbf{n}]$, an external magnetic field, $\mathbf{H}$, couples quadratically to the compo-

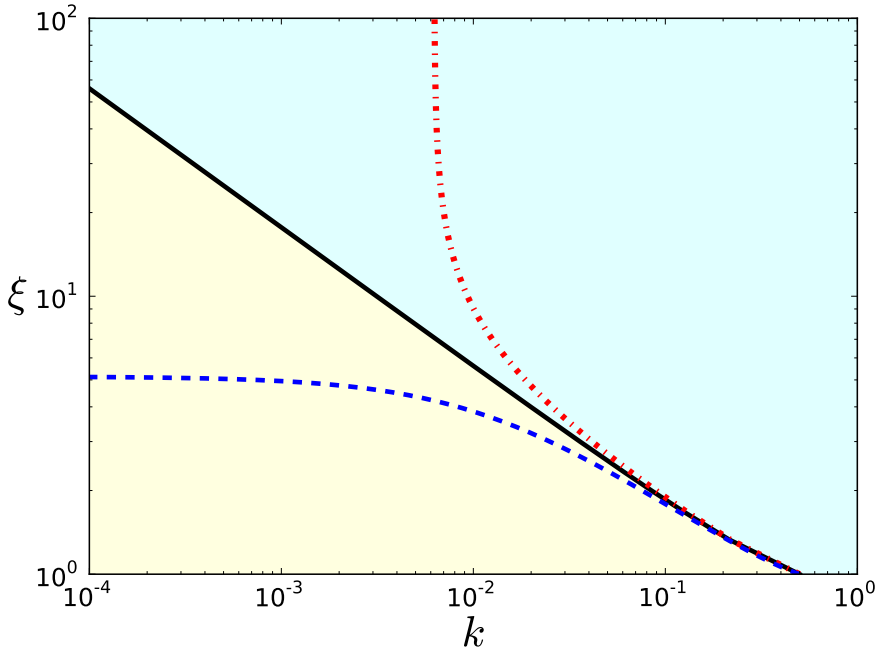

Figure 40: Phase diagram as a function of the toroidal slenderness and the elastic anisotropy in twist and saddle-splay constant, $k \equiv (K_2 - K_{24})/K_3$. The twisted (yellow region) and axial (cyan region) configuration are separated by a boundary line in the absence of an external field (solid black), when $\mathbf{H} = \sqrt{0.1K_3}/(\sqrt{\chi_a}R_2)\,\hat{\boldsymbol{\phi}}$ (dashed blue) and when $\mathbf{H} = \sqrt{0.1K_3}/(\sqrt{\chi_a}R_2)\,\hat{\mathbf{z}}$ (dash-dotted red).

nents of $\mathbf{n}$ rather than linearly as in spin systems. The magnetic free energy contribution reads:

$$F_m = -\frac{\chi_a}{2}\int \mathrm{d}V\,(\mathbf{n}\cdot\mathbf{H})^2\,, \tag{167}$$

where $\chi_a = \chi_\parallel - \chi_\perp$, the difference between the magnetic susceptibilities parallel and perpendicular to $\mathbf{n}$. Consequently, there is no explicit chiral symmetry breaking due to $\mathbf{H}$ as is the case in the Ising model. Rather, $\mathbf{H}$ shifts the location of the critical transition in the phase diagram. For concreteness, we will consider two different applied fields, namely a uniaxial field $\mathbf{H} = H_z\hat{\mathbf{z}} = H_z\sin(\psi)\hat{\mathbf{r}} + H_z\cos(\psi)\hat{\boldsymbol{\psi}}$ and an azimuthal field $\mathbf{H} = H_\phi\hat{\boldsymbol{\phi}}$, as

if produced by a conducting wire going through the hole of the toroid. For $\mathbf{H} = H_z\hat{\mathbf{z}}$ we find

$$\begin{aligned} F_m &= -\pi^2\chi_a H_z^2 R_1 R_2^2 \xi^2 \left(2\xi\left(\xi - \sqrt{\xi^2-1}\right) - 1\right)\omega^2 \\ &\approx -\frac{\pi^2}{4}\chi_a H_z^2 R_1 R_2^2 \omega^2 \qquad \text{if } \xi \gg 1. \end{aligned} \tag{168}$$

For a positive χ_a this energy contribution is negative, implying that a larger area in the phase diagram is occupied by the twisted configuration. The new phase boundary (Fig. 40), which is now a surface in the volume spanned by ξ, k and H_z instead of a line, reads:

$$\begin{aligned} k_c = \Big[&-1 + 9\xi_c^2 - 6\xi_c^4 - 6\xi_c\sqrt{\xi_c^2-1} + 6\xi_c^3\sqrt{\xi_c^2-1} \\ &- \frac{\chi_a \left(H_z\right)_c^2 R_2^2}{K_3}\left(\xi_c^2 - 1\right)\xi_c \\ &\times \left(-2\xi_c + 2\xi_c^3 + \sqrt{\xi_c^2-1} - 2\xi_c^2\sqrt{\xi_c^2-1}\right)\Big] \Big/ \left(4\xi_c^2\right) \\ &\approx \frac{5}{16\xi_c^2} + \frac{\chi_a \left(H_z\right)_c^2 R_2^2}{16K_3} \quad \text{if } \xi \gg 1. \end{aligned} \tag{169}$$

In contrast, an azimuthal field favours the axial configuration, contributing a postive ω^2-term to the energy when $\chi_a > 0$:

$$\begin{aligned} F_m &= -\pi^2\chi_a H_\phi^2 R_1 R_2^2 \\ &+ \frac{2\pi^2}{3}\chi_a H_\phi^2 R_1 R_2^2 \xi \left(2\xi^2\left(\xi - \sqrt{\xi^2-1}\right) - \sqrt{\xi^2-1}\right)\omega^2 \\ &\approx -\pi^2\chi_a H_\phi^2 R_1 R_2^2 + \frac{\pi^2}{2}\chi_a H_\phi^2 R_1 R_2^2 \omega^2 \quad \text{if } \xi \gg 1. \end{aligned} \tag{170}$$

Consequently, this yields a shifted phase boundary (Fig. 40):

$$\begin{aligned} k_c = \Big[&-1 + 9\xi_c^2 - 6\xi_c^4 - 6\xi_c\sqrt{\xi_c^2-1} + 6\xi_c^3\sqrt{\xi_c^2-1} \\ &- \frac{2\chi_a \left(H_\phi\right)_c^2 R_2^2}{3K_3}\left(\xi_c^2 - 1\right) \\ &\times \left(1 + \xi_c^2 - 2\xi_c^4 + 2\xi_c^3\sqrt{\xi_c^2-1}\right)\Big] \Big/ \left(4\xi_c^2\right) \\ &\approx \frac{5}{16\xi_c^2} - \frac{\chi_a \left(H_\phi\right)_c^2 R_2^2}{8K_3} \qquad \text{if } \xi \gg 1. \end{aligned} \tag{171}$$

Similar results (eqs. (168)-(171)) hold for an applied electric field $\mathbf{E}$ instead of a magnetic field; the analog of χ_a is the dielectric anisotropy. There could however be another physical mechanism at

play in a nematic insulator, namely the flexoelectric effect [64, 18]. Splay and bend deformations induce a polarisation

$$\mathbf{P} = e_1 \mathbf{n} \nabla \cdot \mathbf{n} + e_3 \mathbf{n} \times \nabla \times \mathbf{n}, \tag{172}$$

where e_1 and e_3 are called the flexoelectric coefficients. Note that the first term in eq. (172) is irrelevant for the divergence-free *Ansatz*. A coupling of $\mathbf{P}$ with $\mathbf{E}$

$$F_P = -\int dV \mathbf{P} \cdot \mathbf{E} \tag{173}$$

could potentially lead to a shift of the transition. In the particuar case when $\mathbf{E} = E_z \hat{\mathbf{z}} = E_z \sin(\psi)\hat{\mathbf{r}} + E_z \cos(\psi)\hat{\boldsymbol{\psi}}$, however, the ω^2 contribution from eq. (173) vanishes, thus not yielding such a shift.

If we now consider toroidal cholesterics rather than nematics, the chiral symmetry is broken explicitly (Fig. 39). A cholesteric pitch of $2\pi/q$ gives a contribution to the free energy of:

$$F_{cn} = K_2 \, q \int \mathrm{d}V \mathbf{n} \cdot \nabla \times \mathbf{n}. \tag{174}$$

Substituting eq. (156) yields

$$\begin{aligned} F_{cn} &= -8\pi^2 K_2 \, q \, R_1 R_2 \, \xi \left(\xi - \sqrt{\xi^2 - 1} \right) \omega + \mathcal{O}\left(\omega^3\right) \\ &\approx -4\pi^2 K_2 \, q \, R_1 R_2 \, \omega + \mathcal{O}\left(\omega^3\right) \qquad \text{if } \xi \gg 1. \end{aligned} \tag{175}$$

Therefore, at the critical line in the phase diagram spanned by k and ξ, the degree of twist or surface angle scales (for large ξ) with the helicity of the cholesteric as

$$\alpha_{eq} \approx \left(2K_2 R_2 \, q / K_3\right)^{1/3} \sim q^{1/3}. \tag{176}$$

This is the analog scaling relation of $m_{eq} \sim H^{1/3}$ in the mean-field Ising model.

4.3.3 *Results for the two-parameter Ansatz*

Motivated by experiments (see section 4.4), we can introduce an extra variational paramer γ to allow for splay deformations, in addition to ω:

$$n_\psi = \omega \frac{\xi r / R_2}{\xi + \gamma \frac{r}{R_2} \cos \psi}. \tag{177}$$

(Note that eq. (156) is recovered by setting $\gamma = 1$ in eq. (177).) In subsection 4.3.1 analytical results for $\gamma = 1$ were presented. In this subsection we will slightly improve these results by finding the optimal value of γ numerically. First, we discretise the azimuthally symmetric director field in the r and ψ direction. Next, we compute the Frank free energy density (eq. (141)) by taking finite differences [25] of the discretised nematic field. After summation over the volume elements the Frank free energy will become a function of ω and γ for a given set of elastic constants and a given aspect ratio. Because of the normalisation condition on $\mathbf{n}$, the allowed values for ω and γ are constrained to the open diamond-like interval for which $-\xi < \gamma < \xi$ and $\frac{|\gamma|-\xi}{\xi} < \omega < \frac{\xi-|\gamma|}{\xi}$ holds.

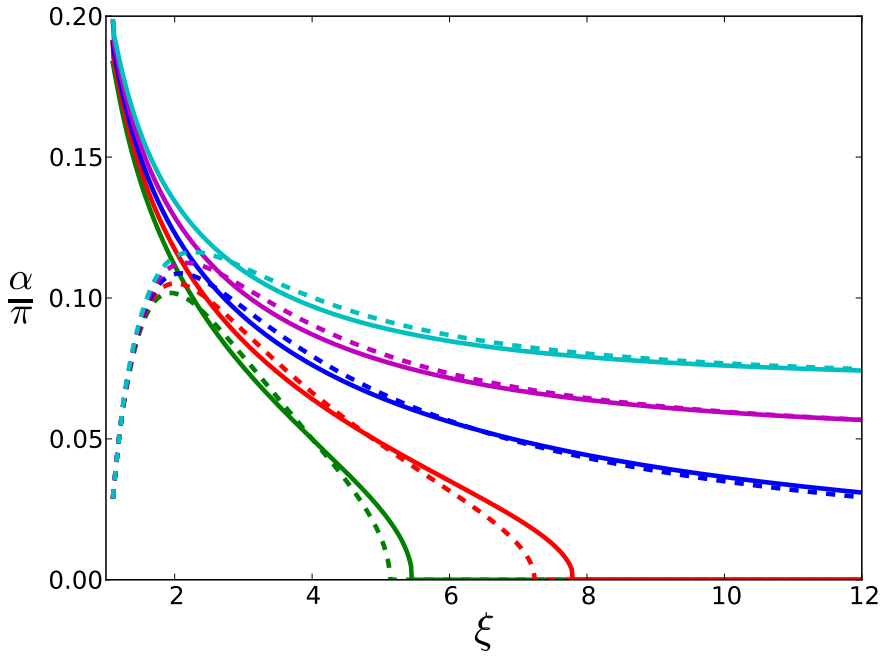

Figure 41: Twist angle α (in units of π) at $\psi = \pi/2$ versus the slenderness ξ for $k = 0.012$ (green), $k = 0.006$ (red), $k = 0$ (blue), $k = -0.006$ (magenta) and $k = -0.012$ (cyan). The dashed lines represent α for $\gamma = 1$, the solid lines represent α found for the optimal γ.

The minima of the energy surface can be found by employing the conjugate gradient method. We have looked at the difference between the $\gamma = 1$ case and the case where the value of γ is chosen to minimise the energy. This was done for various choices of k. We have chosen the material properties of 5CB, *i.e.* $K_1 = 0.64K_3$ and $K_2 = 0.3K_3$ [40]. The value for of K_{24} has not been so accurately

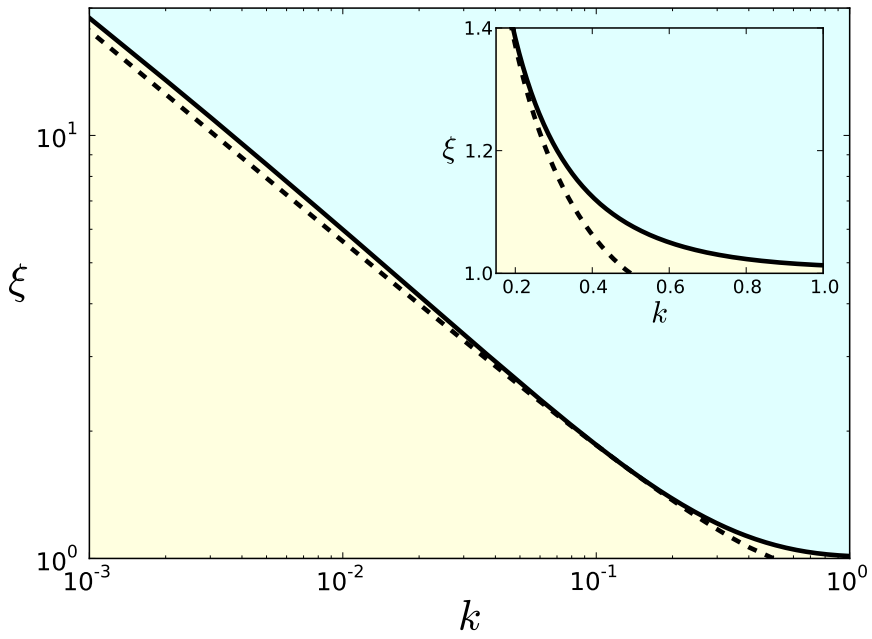

Figure 42: The phase boundary as a function of the toroidal slenderness ξ and elastic anisotropy k for γ as a variational parameter(solid) and for $\gamma = 1$ (dashed). The inset zooms in on the phase boundary for small ξ.

determined, but previous measurements [2, 45, 79, 92, 46, 77] seem to suggest that $K_{24} \approx K_2$, corresponding to $k \approx 0$.

We are interested in how the phase boundary changes by introducing the variational parameter γ. Therefore, the twist angle α, evaluated at the surface of the torus at $\psi = \frac{\pi}{2}$, versus the slenderness ξ is shown in Fig. 41. For the particular choices of k there are two noticeable differences between the single-parameter *Ansatz* and the two-parameter *Ansatz*. Firstly, for small values of ξ, α is changed significantly. Secondly, for larger values of ξ we see that if there is a chiral-achiral phase transition, ξ_c is shifted by a small amount. In Fig. 42 we further investigate how introducing γ influences the phase boundary, by plotting the phase boundary as a function of the toroidal slenderness ξ and elastic anisotropy k for both γ as a variational parameter (solid) and for $\gamma = 1$ (dashed). Observe that, for both the small ξ and small k regime, the difference is significant.

4.4 COMPARISON WITH EXPERIMENT

To make nematic toroidal droplets, Alberto Fernandez-Nieves and co-workers inject a nematic liquid crystal, namely 4-n-pentyl-4'-cyanobiphenyl (5CB), through a needle into a rotating bath containing a yield-stress material consisting of (i) 1.5 wt% polyacrylamide microgels (carbopol ETD 2020), (ii) 3 wt% glycerin, (iii) 30 wt% ethanol, (iv) 1 wt% polyvinyl alcohol (PVA), and (v) 64.5 wt% ultrapure water [77]. The presence of PVA guarantees degenerate tangential (or planar) anchoring for the liquid crystal at the surface of the droplets; they confirmed this by making spherical droplets and checking their bipolar character. We also note that the continuous phase is neutralized to pH 7, where the sample transmission is more than 90% [13]. However, the most relevant property of this phase is its yield stress, σ_y. During formation of the torus, the stresses involved are larger than σ_y and hence the continuous phase essentially behaves as if it were a liquid. The combination of the viscous drag exerted by the outer phase over the extruded liquid crystal and its rotational motion causes the liquid crystal to form a curved jet, as shown in Fig. 43a, which eventually closes onto itself, resulting in a toroidal nematic droplet, such as that shown in Fig. 43b in bright field and in Fig. 43c between cross-polarizers. Once the torus has been formed, the elasticity of the continuous phase provides the required force to overcome the surface tension force that would naturally tend to transform the toroidal droplet into a spherical droplet [76]. Remarkably, when these droplets are observed along their side view under cross-polarizers, their central region remains bright irrespective of the orientation of the droplet with respect to the incident polarization direction, as shown in Fig. 43d-f; the corresponding bright-field images are shown in Fig. 43g-i. Note that for an axial torus with its director field along the tube, the cross-polarized image should appear black for an orientation of 0° and 90° with respect to the incident polarization direction. Hence our result is suggestive of a twisted structure. In fact, twisted bipolar droplets also have a central bright region, when viewed between cross-polarizers, irrespective of their orientation [109, 47, 22, 112].

We then quantify our results by measuring the twist angle in our toroidal droplets along the z direction, from ($r = R_2$, $\psi = 90°$) to

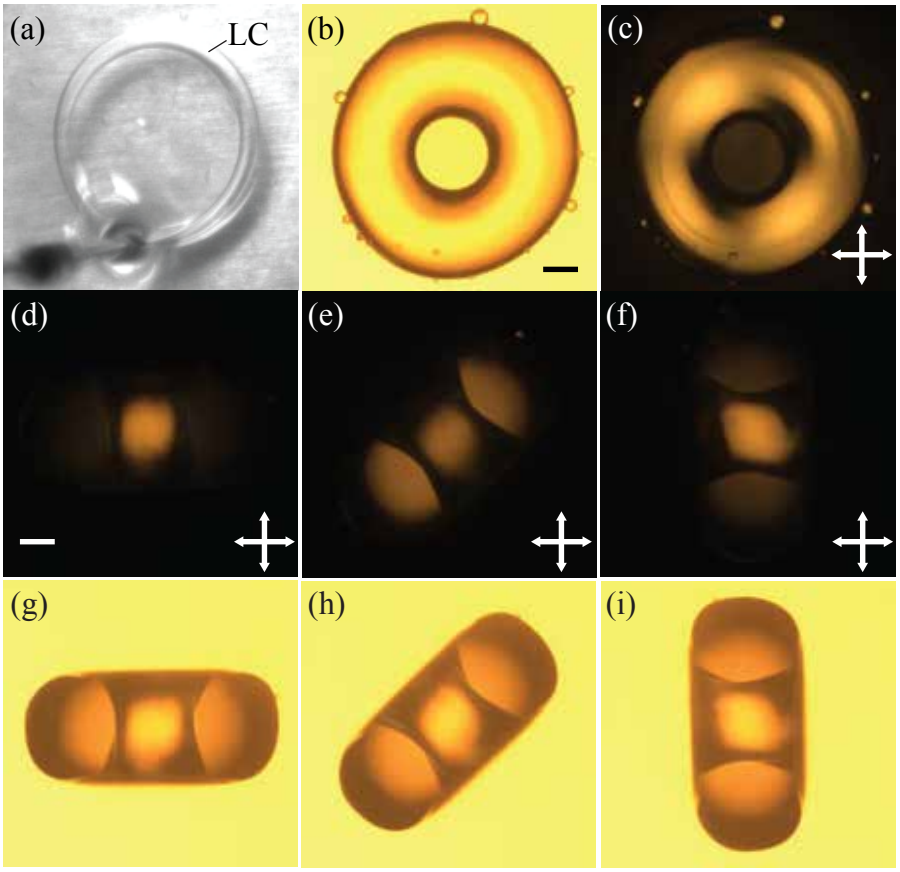

Figure 43: Toroidal droplets. (a) Formation of a toroidal liquid crystal droplet inside a material with yield stress. (b and c) The top view of a typical stable toroidal droplet of nematic liquid crystal is shown in (b) when viewed in bright field and in (c) when viewed under cross-polarizers. (d-f) Side view of a typical toroidal droplet with $\xi = 1.8$ when viewed under cross-polarizers for orientations of 0°, 45°, and 90° with respect to the incident polarization direction. Note that the center part of the toroid remains bright irrespective of its orientation. (g-i) Corresponding bright-field images. The dark regions of the toroid in these images are due to light refraction. (Scale bar: $100\mu m$.) Ref. [77].

($r = R_2$, $\psi = 270°$) (see Fig. 37). The method relies on the fact that linearly polarized light follows the twist of a nematic liquid crystal if the polarization direction is either parallel or perpendicular to the nematic director at the entrance of the sample, provided the Mauguin limit is fulfilled [115]; the corresponding mode of propagation is referred to as extraordinary or ordinary waveguiding, respectively. We then image the torus from above (Fig. 44A), rotate the polarizer to ensure that the incident polarization direction is parallel or perpendicular to the nematic director at ($r = R_2$, $\psi = 90°$), and then rotate the analyzer an angle ϕ_{exit} with respect to the polarizer while monitoring the transmitted intensity, T. The minimum in T, shown in Fig. 44B, reflects the lack of light propagation through the analyzer, indicating that the incident polarization direction has rotated an amount τ such that it is perpendicular to the analyzer after exiting the torus at ($r = R_2$, $\psi = 270°$). The image of the torus in this situation exhibits four black regions where extinction occurs, as shown in Fig. 44C; these correspond to waveguiding of ordinary and extraordinary waves. It is along these regions that we measure T. The counterclockwise rotation of the incident polarization direction by an angle of $-56°$ exactly corresponds to the twist angle of the nematic along the z direction through the center of the circular cross section. However, to increase the precision of our estimate, we fit the T vs. ϕ_{exit} results to the theoretically expected transmission [115], leaving τ as a free parameter. We find $\tau = (52.9 \pm 0.4)°$ for $\xi = 3.5$. Moreover, within the experimentally accessed ξ-range, we find that the twist is nonzero and that it monotonously decreases with increasing aspect ratio, as shown in Fig. 44D. Remarkably, these features are captured by our theoretical calculations for large ξ, as shown by the dashed line in Fig. 44D. We note that the deviations of the experiment and the theory for small ξ result from the inadequacy of the *Ansatz* in describing the highly twisted structures observed experimentally at these low values of ξ. This can be partially resolved by lifting the constraint that $\gamma = 1$. This introduces a second variational parameter in the *Ansatz*, which allows the nematic field to splay. The result qualitatively captures the experimental trend for all aspect ratios, as shown by the solid line in Fig. 44D. By further comparing the experiment to the theory in the high ξ-region, we obtain a value for the saddle-splay elastic

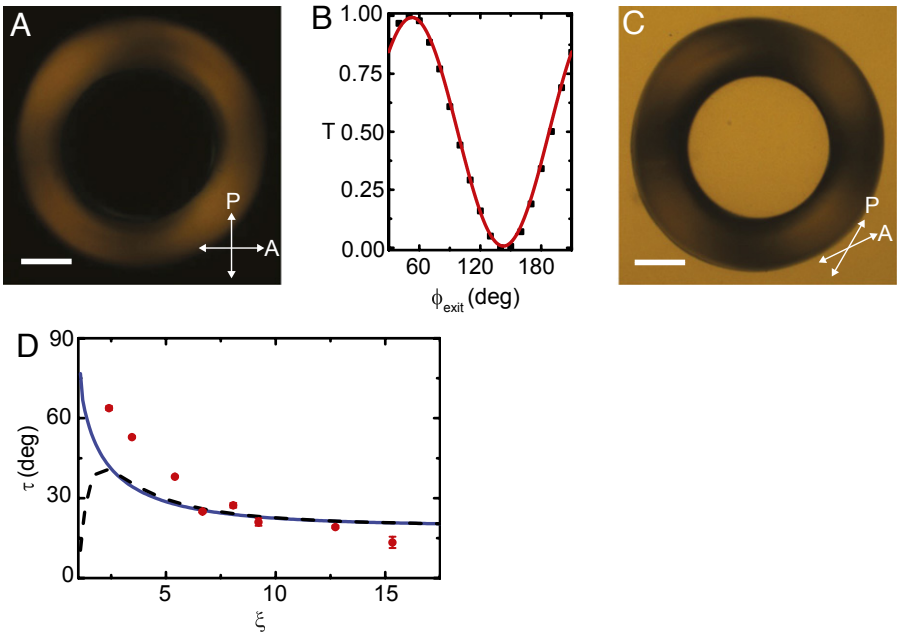

Figure 44: Determination of the twist angle and its dependence with slenderness. (A) A torus with $\xi = 3.5$ when viewed from the top and between crosspolarizers. (B) Transmission, T, as a function of the angle between the incident polarization direction and the analyzer, ϕ_{exit}. The line is a fit to the theoretical expectation in the Mauguin limit [115] with the twist angle, τ, as the only free parameter. We obtain $\tau = (52.9 \pm 0.4)°$. (C) Top view of the same torus at the minimum of the transmission curve. We measure T along the four black regions that are observed, which are darkest for the indicated direction of the polarizer and analyzer. The sense of rotation of the analyzer indicates the nematic arrangement is right-handed; this likely results from the way the torus is generated, as all tori generated in the same way have the same handedness. (D) Twist angle as a function of ξ. The dashed line represents the theoretical prediction based on eq. (156), for $K_{24} = 1.02K_2$. The solid line represents the theoretical prediction based on the improved *Ansatz* including the second variational parameter γ for the same value of K_{24}, where we have used that $K_1 = 0.64K_3$ for 5CB [40]. (Scale bar: $200\mu m$.) Ref. [77].

constant of $K_{24} = 1.02K_2$, which is slightly larger than the twist elastic constant, supporting our interpretation on the relevance of saddle-splay distortions. However, our analysis cannot exclude the possibility of a slightly smaller value of K_{24} and hence of a twisted-to-axial transition for extremely large ξ.

4.5 CONCLUSIONS

We have investigated spontaneous chiral symmetry breaking in toroidal nematic liquid crystals. As in the case of nematic tactoids [80, 101], the two ingredients for this macroscopic chirality are orientational order of achiral microscopic constituents and a curved confining boundary. This phenomenon occurs when both the aspect ratio of the toroid and $\frac{K_2-K_{24}}{K_3}$ are small. The critical behavior of this structural transition belongs to the same universality class as the ferromagnet-paramagnet phase transition in the Ising model in dimensions above the upper critical dimension. The analogues of the magnetisation, reduced temperature and external field are the degree of twist (or surface angle), slenderness or $\frac{K_2-K_{24}}{K_3}$, and (cholesteric) helicity in liquid crystal toroids, respectively. Critical exponents are collected in Table 1.

Liquid crystal toroid	Mean-field Ising model	Exponent
$\alpha_{eq} \sim (-\delta\xi)^{\beta}$	$m_{eq} \sim (-t)^{\beta}$	$\beta = 1/2$
$\alpha_{eq} \sim (-\delta k)^{\beta}$		
$\alpha_{eq} \sim q^{1/\delta}$	$m_{eq} \sim H^{1/\delta}$	$\delta = 3$

Table 1: Dictionary of the critical behavior of the structural transition in liquid crystal toroids and the thermal phase transition in the mean-field Ising model.

Thus, the helicity rather than an external field breaks the chiral symmetry explicitly. Remarkably, since an external field couples quadratically to the director field, it induces a shift of the phase boundary. An azimuthally aligned field favours the mirror symmetric director configuration, whereas a homogeneous field in the z-direction favours the doubly twisted configuration.

A minimization of the elastic energy analogous to the one presented in this article for toroidal droplets, has also been carried out for spherical droplets [112]. The analytical results reproduce qualitatively the twisted textures observed experimentally in spherical bipolar droplets [109]. In this case, detailed measurements of the dependence of the twist angle on the elastic moduli were carried out by changing temperature which in turn affects the elastic moduli. The measured exponent β was 0.75 ± 0.1 for 8 CB and 0.76 ± 0.1 for 8 OCB [47], rather than the $\frac{1}{2}$ exponent we calculated in our mean field energy minimizations that entirely neglect thermal fluctuations.